

What Does FEXI Measure in Neurons?

Valerij G. Kiselev^{1, 2, *} and Jing-Rebecca Li³

¹*Medical Physics, Department of Radiology, University Medical Center Freiburg, Faculty of Medicine, University of Freiburg, Killianstrasse 5a, 79106, Freiburg, Germany*

²*Department of Neurophysics, Max Planck Institute for Human Cognitive and Brain Sciences, Stephanstrasse 1a, 04103 Leipzig, Germany*

³*Inria-Saclay, Equipe Idefix, UMA, ENSTA Paris, Institut Polytechnique de Paris, 91120, Palaiseau, France.*

Exchange between tissue compartments is crucial for interpretation of diffusion MRI measurements in brain gray matter. Reported values of exchange time are broadly dispersed, about two orders of magnitude. We analyze the measurement technique called Filtered Exchange Imaging (FEXI) using numerical solution of Bloch–Torrey equation in digitalized neurons downloaded from NeuroMorpho.org. The FEXI outcome, the recovery of diffusion coefficient in cells with impermeable membrane is multiexponential, tightly related to the eigenvalues of the Laplace operator. Fitting the commonly used exponential recovery function results in a strong dependence of the apparent exchange time τ_x on the involved mixing time interval. For short mixing times, τ_x is of the order of 10 ms. It gets an order of magnitude larger for mixing times of a few hundreds of milliseconds. To obtain an estimate of membrane permeability, κ , we reinterpret previously published data on preeexchange lifetime in neuronal cell culture. It results in $\kappa \approx 0.005 \mu\text{m}/\text{ms}$. The corresponding exchange time $\tau_x \approx 140$ ms. We conclude that essentially shorter exchange times are due to fast geometric exchange inside the ramified cells.

I. INTRODUCTION

Diffusion MRI has been successfully applied for evaluating the microstructure of brain white matter [1]. Extension of this approach to gray matter is challenged by exchange with extracellular space. Nulling the advantage of well-defined compartments, exchange comes in the focus of today’s research. Among a number of approaches, filter exchange imaging (FEXI) [2–4] appears a rather straightforward way to evaluate exchange between compartments with slow and fast diffusion, Fig. 1. This impression can be however deceptive because the measurement is sensitive to both the genuine exchange via the permeation through cellular membranes and to geometric exchange within the same cell [4–7]. The latter takes place in cells with complex, tortuous geometry in which the filter, a strong diffusion weighting, does not affect nuclear spins with restricted mobility in the direction of the filter gradient. During the mixing time, these spins diffuse in regions inside the same cell without such restrictions thus contributing in the observed recovery of diffusion coefficient.

In this paper, we scrutinize the outcome of FEXI in realistic neurons focusing on the geometric exchange inside the same cells. The cell membranes are first treated impermeable. We consider a simple model of long cylinder bent at the right angle to clarify the relation of the apparent exchange time with the eigenmodes of Laplace operator. On the next step, we find the membrane permeabil-

ity by matching in silico results for the preeexchange lifetime with published experimental data [8]. The resulted value is used to simulate FEXI outcome in permeable cells, yet with idealized extracellular space.

II. METHODS

Three skeleton descriptions of neurons were downloaded from the public repository NeuroMorpho.org [9, 10], in SWC format. Then `Alpha_Mesh_Swc` [11], an automatic and robust surface mesh generator for SWC files, was used to generate a three dimensional surface mesh for each cell, which was then used by the tetrahedral mesh generator `tetgen` [12] to create a simulation-ready finite elements mesh. See Table I and Fig. 2 for descriptions of the three cells. The evolution of nuclear magnetization inside the cells was calculated with the diffusion MRI simulation software `SpinDoctor` to solve the Bloch–Torrey equation using the finite-element method [13, 14]. In particular, the Numerical Matrix Formalism method was utilized since many simulations were needed in the same geometries [15].

The simulated FEXI weighting included the following parameters (Fig. 1). Both the filter and the detection blocks used the Stejskal–Tanner diffusion weighting with rectangular gradient pulses of magnitude $g_f = 750 \text{ mT}/\text{m}$. For the filter, the gradient pulse duration was $\delta_f = 4 \text{ ms}$ with the interpulse interval $\Delta_f = 5 \text{ ms}$. This resulted in $b_f = 2.36 \text{ ms}/\mu\text{m}^2$. The timing of the detection block was $\delta_d = 1 \text{ ms}$ and $\Delta_d = 2 \text{ ms}$ ($b_d = 0.067 \text{ ms}/\mu\text{m}^2$). Being realistic for preclinical scanners, this choice ap-

* Corresponding author: kiselev@ukl.uni-freiburg.de

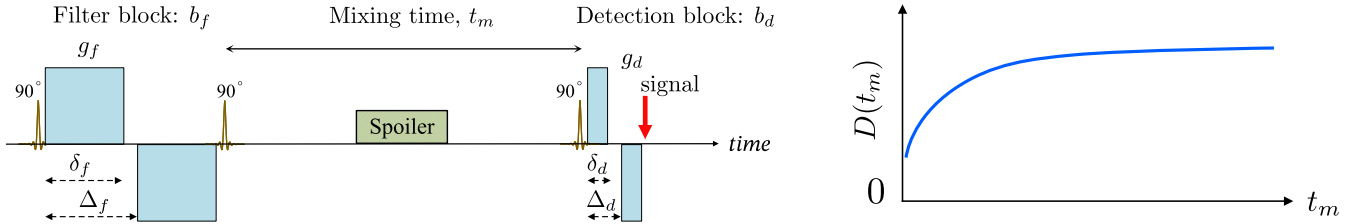


FIG. 1: Left: Schematics of FEXI as implemented in this study. Wide gradient pulses are used as the most realistic approach. Right: The anticipated recovery of diffusion coefficient with the increasing mixing time.

proaches the requirement of instant diffusion weighting, which largely simplifies the analysis. The bulk water diffusivity inside the cell was set to $D_0 = 2 \mu\text{m}^2/\text{ms}$ [16]. The above parameters serve as the default unless stated otherwise.

The direction of the filter and detection gradients were selected along the eigenvectors of cell's diffusion tensor D_{ab} . The tensors were found for each cell assuming impermeable membranes and using the detection block gradients applied in 32 directions distributed on a semi-sphere. It was important for the data consistency to use the same timing as in the detection block, since D_{ab} sharply depends on time due to the contribution of narrow subcompartments within the cells. The eigenvectors and eigenvalues of D_{ab} are summarized in Table I. The mixing time t_m was the main variable in the simulations ranging from 5 ms to 10 s in the absence of any background relaxation.

To enable a semi-analytical analysis, we considered FEXI in a radically simplified geometry of a bent cylinder. It was created as a union of two equal cylinders joined at their ends at the right angle (Fig. 2). The radius of both parts was $\rho = 1 \mu\text{m}$ and the length $L/2$, with the total length $L = 200 \mu\text{m}$ roughly matching the maximum dimension of cells.

For the evaluation of cell membrane permeability, we used the SpinDoctor for modeling the magnetization leakage from cells to extracellular space. The information carrier was the transverse magnetization, since it is the quantity SpinDoctor works with. The digitized cells were embedded in large rectangular boxes representing extracellular space. The initial magnetization there was zero and a very short $T_2 = 0.1 \text{ ms}$ simulated the spin removal in the real experiment [8]. The initial magnetization inside the cells was constant with no inherent relaxation.

The obtained membrane permeability was used to discuss the exchange with ECS using a semi-analytical approach. The magnetization leakage in large ECS was recalculated to find fractions of migrating spins for realistic ECS volume using the Kärger exchange model. Each spin migration group was assigned a contribution in the overall diffusion coefficient, either numerically or analytically as explained below.

III. RESULTS: IMPERMEABLE CELLS

The solution of Bloch–Torrey equation was set to have 10^{-4} relative tolerance and 10^{-6} absolute tolerance for the ODE solver. The relative magnitude of the imaginary part of the signal, theoretically a real quantity, was about 10^{-5} , in agreement with the predefined tolerance. The major error was due to the limited size of finite elements mesh. For example, an about 10-fold test increase in the mesh size in cell 2 (from 14×10^3 to 142×10^3) resulted in an 1% effect, while significantly increasing the computation time.

The FEXI results for all three cells are shown in Fig. 3 along with the fitted recovery equation

$$D(t_m) = D_\infty - a e^{-t_m/\tau_x} \quad (1)$$

with adjustable D_∞ , a and τ_x (in what follows, we denote all exchange times with τ and the corresponding rates with $r = 1/\tau$). A systematic deviation of the fitted lines from the data is evident for all cells. A similar pattern was reported in our previous simulations in porous media [7]. This deviation is visualized in Fig. 4 as the dependence of the apparent exchange time, τ_x on the interval of mixing time, t_m , used for fitting. Fitting to the first three data points for $t_m = 5, 10, 20 \text{ ms}$ results in $\tau_x = 12 \text{ ms}$. Using the full t_m range up to 10 s gives $\tau_x \approx 1500 \text{ ms}$. Of course, such long t_m 's are only available in simulations. Practically relevant are the values of a few hundred of milliseconds. As an example, we obtain $\tau_x = 156 \text{ ms}$ for the mixing time up to $t_m = 320 \text{ ms}$, which is an order of magnitude larger than the result for the shortest t_m .

To interpret this result, consider a largely simplified geometry of a cylinder bent 90° in the middle, Fig. 2. Solution of the Bloch–Torrey equation gives the result shown in Fig. 5. Fitting Eq. (1) demonstrates the same deviation pattern as for all cells. This similarity motivates scaling the analysis from the simplest model to cells, as discussed below.

The simplest theory treats the filter and the detection blocks instant. The calculations are then focused on the magnetization evolution during the mixing time. This problem is effectively one-dimensional as long as $\rho \ll L$ and we use the coordinate x for the whole cylinder length.

	cell 1	cell 2	cell 3
type, references	03b_spindle7aACC.CNG [17]	02a_pyramidal2aFI.CNG [17]	1-10-10.CNG [18]
e_x	0.0086 0.6595 -0.7516	0.6073 0.6703 0.4264	-0.2385 0.9467 0.2163
e_y	0.0059 0.7516 0.6596	-0.0603 -0.4963 0.8661	-0.1277 -0.2514 0.9594
e_z	0.9999 -0.0101 0.0025	0.7922 -0.5517 -0.2610	0.9627 0.2012 0.1809
λ/D_0	0.6468 0.7496 0.8276	0.7577 0.7965 0.8660	0.6915 0.7109 0.8110

TABLE I: Specification of cells used in this study, eigenvectors of diffusion tensors (columns) and the corresponding eigenvalues.

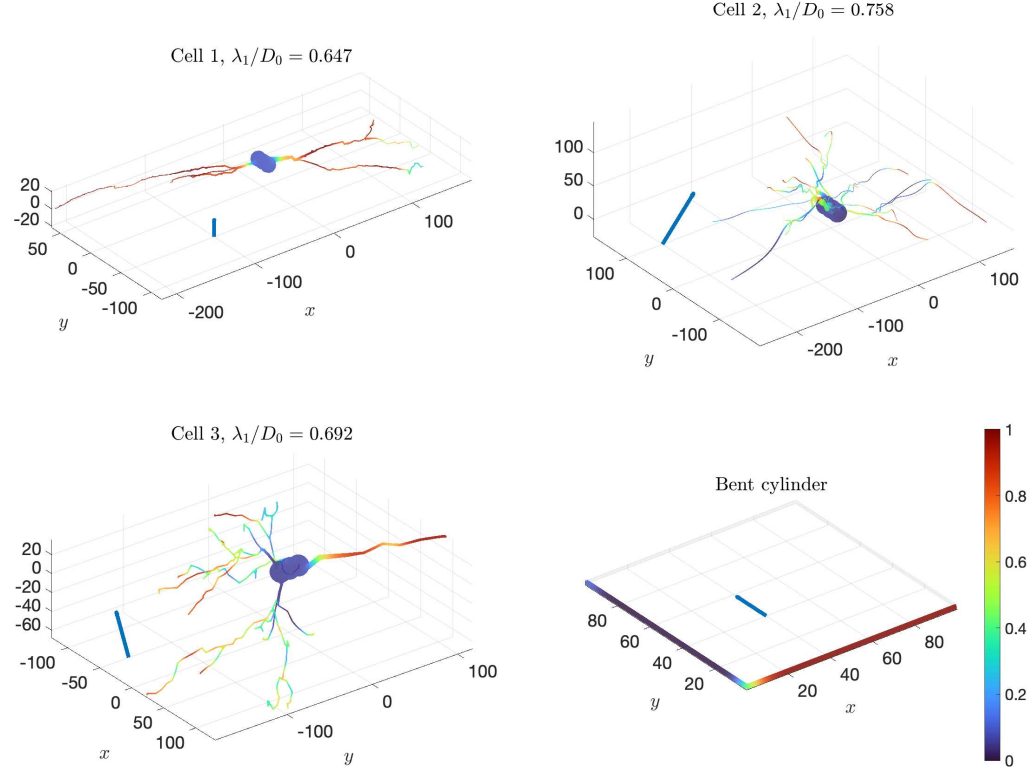


FIG. 2: The three cells used in this study (Table I) and a simple model of a bent cylinder. The colors encode the signal magnitude right after the filter. To cells, the filter gradient was applied along the eigenvectors with the smallest eigenvalues λ_1 , the directions shown with the blue lines. For the cylinder, the direction was along the y -axis.

Let the filter and the detection gradient be applied parallel to one of shoulders of the bent cylinder, say for $-L/2 < x < 0$ (this section is $-y$ in Fig. 2). The evolution then starts with the magnetizations

$$\psi_{\parallel}^{(0)} = e^{-b_f D_0}, \quad \psi_{\perp}^{(0)} = 1 \quad (2)$$

in the parallel and orthogonal shoulder, respectively. The approximation $\psi_{\perp}^{(0)} = 1$ indicates the neglect of diffusion across the thin cylinder. The first assignment is also an approximation that neglects the transition zone around $x = 0$ and the edge enhancement, which can be barely recognized for $y \gtrsim 90 \mu\text{m}$ in Fig. 2. The initial magnetization gradually evens out forming a smooth function $\psi(t, x)$. The detection block measures the diffusion coefficient D_0 in the parallel shoulder and zero in the orthogonal one. The weights of these shoulders in the overall

diffusivity $D(t)$ are proportional to their contributions to the normalized signal, $S = S_{\parallel} + S_{\perp}$, where

$$S_{\parallel}(t) = \frac{1}{L} \int_{-L/2}^0 dx \psi(t, x), \quad (3)$$

$$S_{\perp}(t) = \frac{1}{L} \int_0^{L/2} dx \psi(t, x). \quad (4)$$

In terms in this quantities,

$$\frac{D(t)}{D_0} = \frac{S_{\parallel}(t)D_{\parallel} + S_{\perp}(t)D_{\perp}}{[S_{\parallel}(t) + S_{\perp}(t)]D_0} \approx \frac{S_{\parallel}(t)}{S_{\parallel}(t) + S_{\perp}(t)}. \quad (5)$$

The evolution of $\psi(t, x)$ during the mixing time is found routinely using the decomposition in the eigenfunctions

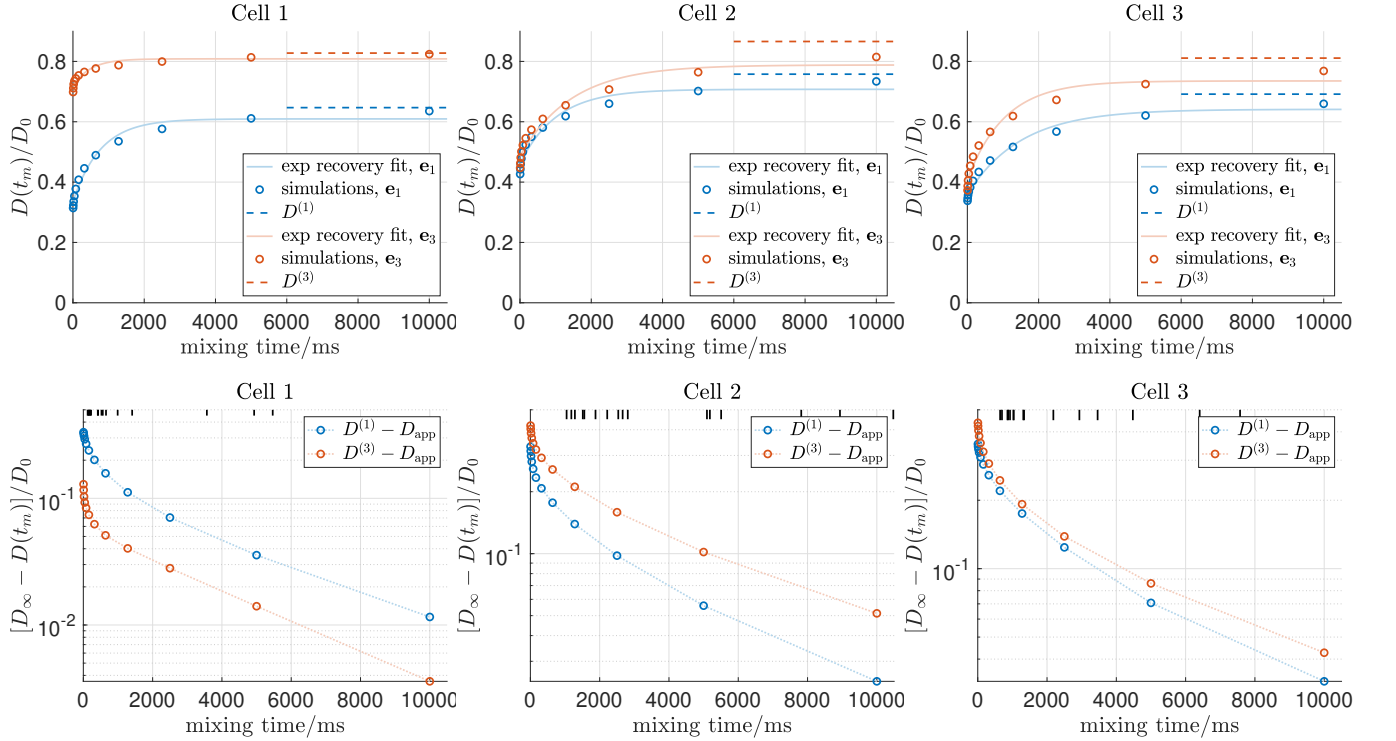


FIG. 3: The recovery of diffusion coefficient as a function of mixing time for all cells. Diffusion-weighting gradients in the filter and detection block were applied along the eigenvectors, $\mathbf{e}_{1,3}$, with the smallest and largest eigenvalues, λ_1 and λ_3 , respectively. Top row: The solid lines show $D(t_m)$, Eq. (1), fitted to data obtained via the solution to the Bloch–Torrey equation (circles). The dashed lines indicate the undisturbed values of $D(\infty)$, which are the corresponding eigenvalues of diffusion tensor. Bottom row: The approach of $D(t_m)$ to its undisturbed values. The ticks at the frame top show the time $\tau_n = 1/\lambda_n$ corresponding to 16 numerically found [19] lowest nonzero eigenvalue of Laplace operator $D_0 \nabla^2$, Eq. (A1). The value $\tau_1 = 14$ s for cell 3 is outside the plot range.

of the Laplace operator, see Appendix A 1. The result is

$$S_{\parallel}(t) = \frac{\psi_{\perp}^{(0)} + \psi_{\parallel}^{(0)}}{4} - \frac{4(\psi_{\perp}^{(0)} - \psi_{\parallel}^{(0)})}{L^2} \sum_{n=1}^{\infty} \frac{e^{-D_0 k_n^2 t}}{k_n^2}, \quad (6)$$

$$S_{\perp}(t) = \frac{\psi_{\perp}^{(0)} + \psi_{\parallel}^{(0)}}{4} + \frac{4(\psi_{\perp}^{(0)} - \psi_{\parallel}^{(0)})}{L^2} \sum_{n=1}^{\infty} \frac{e^{-D_0 k_n^2 t}}{k_n^2}, \quad (7)$$

where $k_n = (2n - 1)\pi/L$. The exponential functions describe the leveling off of the initial magnetizations, $\psi_{\perp}^{(0)}$ and $\psi_{\parallel}^{(0)}$; the two expressions become equal at $t \rightarrow \infty$. The terms with the series cancel in the whole signal, $S(t) = (\psi_{\perp}^{(0)} + \psi_{\parallel}^{(0)})/2$, for any time reflecting the absence of relaxation in the present consideration.

The resulted diffusion coefficient, $D(t_m)$, which is calculated according to Eq. (5), is shown in Fig. 5. The agreement with the numerically calculated values is good giving the simplicity of the theory. For short times, $\sqrt{D_0 t_m} \ll L$, the partial signals can be found in the closed form (appendix A 2), Fig. 5

$$S_{\parallel,\perp}(t) = \frac{1}{2}\psi_{\parallel}^{(0)} \pm (\psi_{\perp}^{(0)} - \psi_{\parallel}^{(0)})\sqrt{\frac{Dt}{\pi L^2}}. \quad (8)$$

Equation (5) then gives

$$\frac{D(t)}{D_0} = \frac{\psi_{\parallel}^{(0)}}{\psi_{\perp}^{(0)} + \psi_{\parallel}^{(0)}} + \frac{\psi_{\perp}^{(0)} - \psi_{\parallel}^{(0)}}{\psi_{\perp}^{(0)} + \psi_{\parallel}^{(0)}} \sqrt{\frac{4Dt}{\pi L^2}}. \quad (9)$$

Note that this expression is more general than the zero-order approximation in Eq. (2). The result can be improved by accounting for diffusion in the orthogonal section. In particular, for short times the two terms in the numerator in the middle expression in Eq. (5) can be comparable, which promotes the effect of small diffusivity in the orthogonal shoulder. Such an improvement is outside the scope of this paper as we focus on a qualitative understanding of diffusion recovery in neurons.

The main lesson from the above analysis is that the recovery of diffusion coefficient is substantially multiexponential, Eqs. (6) and (7). It is well evident in the bottom row in Fig. 3. This behavior contrasts with commonly implied Eq. (1), which describes the true transcytoleminal exchange provided a well-mixed magnetization inside the cell [20]. This discrepancy explains the poor fitting of this equation. The interplay of many exponentials for short times can result in a specific functional dependence (e.g., $\sim \sqrt{t_m}$ for the bent cylinder, Eq. (9)). Note that this approximation might be sufficient for practical measurement in which t_m is limited by the longitudinal relax-

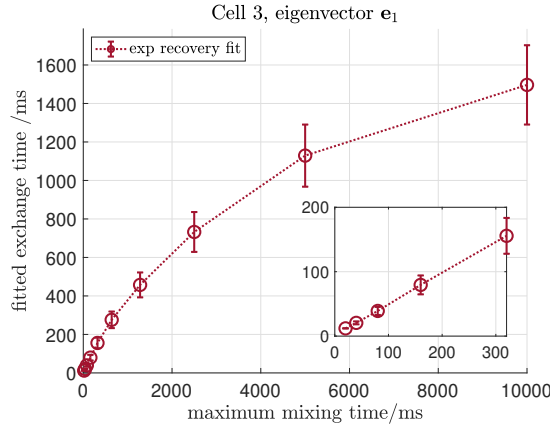


FIG. 4: Fitted apparent exchange time, τ_x , as a function of the mixing time range for one cell. The fitting was performed from the minimum t_m to the value indicated on the axis. The inset shows the practically relevant range of t_m . The first value for $t_m = 20$ ms is $\tau_x = 12$ ms.

ation. The crossover between the short and long times is set by the smallest nonzero eigenvalue of the Laplace operator, $t_m \sim 1/\lambda_1$, where $\lambda_1 = \pi^2 D_0/L^2$ for the cylinder (it defines the first terms in the series in Eqs. (6) and (7)). For the considered parameters, $D_0 = 2 \mu\text{m}^2/\text{ms}$ and $L = 200 \mu\text{m}$, this time is about 2000 ms, which is supported by data shown in Fig. 5 in which the short-time approximation ceases to work around this time.

This consideration suggests the semilogarithmic scale for presenting the approach of diffusion coefficient to its asymptote, $D_\infty - D(t_m)$, which is shown in the bottom row of Fig. 3 for all cells. A similar dependence for the bent cylinder is shown in Fig. 6. Initial rapid decrease in the difference $D_\infty - D(t_m)$ gradually tends to a straight line indicating the trend to the monoexponential attenuation, which is governed by the smallest nonzero eigenvalue of Laplace operator. This is very precise for the cylinder with its simple eigenvalue spectrum. The slope found from the data plotted in Fig. 6 is $-0.51 \times 10^{-3} \text{ ms}^{-1}$, which agrees well with the first nonzero eigenvalue $\lambda_1 = \pi^2 D_0/L^2 = 0.49 \times 10^{-3} \text{ ms}^{-1}$. The above crossover time is the inverse of these quantity. Note that the next eigenvalue is 9 times larger, Eq. (A2), corresponding to 220 ms characteristic time, well in the range where the monoexponential attenuation sets up in Fig. 6.

The monoexponential behavior for long times is also obvious for cell 1 due to its relatively simple geometry. Two other cells with more developed dendritic trees show a similar trend, but less accurately. It can be explained by the presence of multiple smaller eigenvalues that result in larger time constants, Fig. 3. Pursuing this relation quantitatively is beyond the scope of this work because it requires the detailed geometry of eigenfunctions [19].

Another problem for the translation from the cylinder model to ramified cells is the contribution of the localized

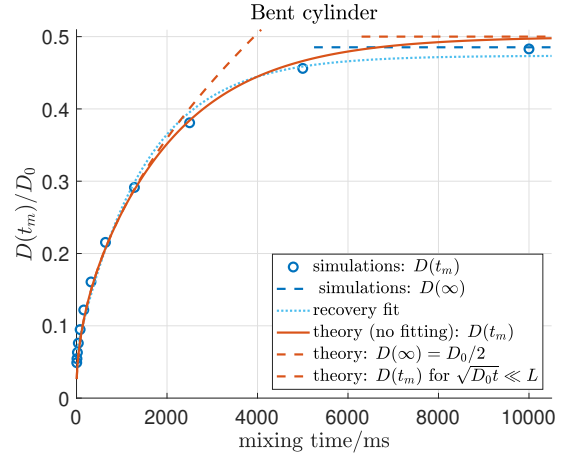


FIG. 5: Recovery of diffusion coefficient as in the top row of Fig. 3, here for the bent cylinder shown in Fig. 2 (circles). It is compared with the analytical result in the form of a series over the eigenvalues of the Laplace operator, Eq. (5) (solid line). The dashed lines show the prediction of the simplified theory for the unperturbed diffusivity and the short-time closed asymptotic form for $\sqrt{D_0 t} \ll L$, Eq. (9). All calculations were performed assuming the approximation of Eq. (2).

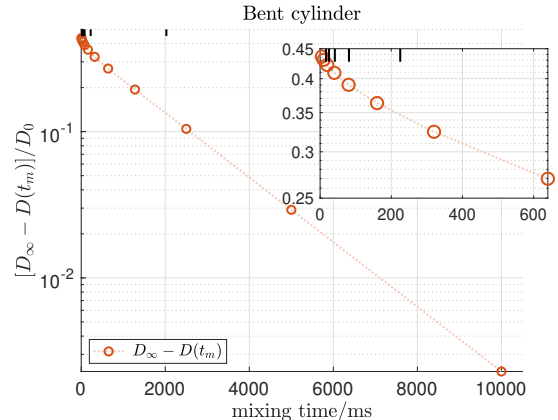


FIG. 6: The approach of $D(t_m)$ to its undisturbed asymptote as in the bottom row of Fig. 3, here for the bent cylinder. The black ticks on the top have the same meaning as in Fig. 3 for the first 6 time constants.

soma, which takes 82%, 77% and 77% of volume for the three cells, respectively.

IV. DISCUSSION

A. Mismatch in Exchange Times

Exchange time has been targeted in a number of diffusion MRI experiments. The results are widely, two orders of magnitude, dispersed, see Fig. 1 and Table S1 in Ref. [21] for an overview. An obvious reason for such a dispersion is the variety of objects, methods and targeted quantities. Focusing on the fast-exchange side of the re-

ported spectrum, the exchange time reaches a few tens of millisecond. In particular, a thorough recent study [22] reported the median value $\tau_x = r_x^{-1} = 13$ ms (using an other method, not FEXI). This time is surprisingly short, which motivates a deeper look into different measurement techniques. The central quantity is the membrane permeability, which we estimate in the next section. While the above results are precise, the following consideration suffers from insufficient data such as missing details about experimental cells. The obtained figures are therefore only plausible estimates, which suggests putting it in Discussion rather than the result section.

B. Membrane permeability

Focusing on geometric exchange, we treated the cell membrane impermeable. Direct measurement of membrane permeability are scarce. To get an idea about the actual values, erythrocytes, which belong to the most permeable cells, have a membrane with $\kappa = 0.06 - 0.07 \mu\text{m}/\text{ms}$ at the body temperature [23, 24]. Neural cells were subjected to the osmotic challenge in a few studies. The results are controversial, from undetectable [25] to the value $\kappa = 0.047 \mu\text{m}/\text{ms}$ [26].

We focus now on experimental data for the preechange lifetime in neural cells, which is straightforward to interpret. We denote it with τ_{io} , (the index implies the transition “inside \rightarrow outside”). The main idea of the measurement is to suppress the signal from extracellular space and monitor the decrease in the intracellular signal. The suppression can be imposed by doping the extracellular space with a paramagnetic contrast agent [27, 28]. This method can be questioned due to possible interplay of the observed inversion recovery with the contrast agent-induced magnetic field inside the cells. This issue was absent for viable neural cell grown on glass microbeads for which the magnetization in extracellular space was removed with mechanical flow of perfusate [8]. The results of three studies were $\tau_{io} = 550$ ms in the rat brain [27], $r_{io} = 2.0 \pm 1.7 \text{ s}^{-1}$ for the rat brain cortical cultures [28] and $\tau_{io} = 750 \pm 50$ ms for neurons and $\tau_{io} = 570 \pm 30$ ms for astrocytes [8]. With a reasonable agreement between each other, these values are more than an order of magnitude larger than those obtained with diffusion MRI [22].

To analyze the mismatch between the two approaches, we first need to realize the difference between the exchange time and preechange lifetimes. Both notions rely on the standard exchange model between well-mixed compartments with M_i and M_o being the amount of water in the slow and fast compartment, respectively [29],

$$\begin{aligned} \frac{dM_i}{dt} &= -r_{io}M_i + r_{oi}M_o \\ \frac{dM_o}{dt} &= +r_{io}M_i - r_{oi}M_o. \end{aligned} \quad (10)$$

Since the equilibrium occurs for equal concentrations, the transition rates obey the condition $v_i r_{io} = v_o r_{oi}$, where v_i and v_o are the volume fractions of two compartments.

When used in the MRI context, these equation are supplemented with characteristics of two compartments such as distinguished relaxation rates or diffusivities. The quantities M_i and M_o become then the signal fractions, the fractions of water multiplied with its specific signal contribution. Experiments with the suppressed extracellular signal correspond to the case $M_o = 0$, which means that the measured quantity is r_{io} . Diffusion MRI measures the bidirectional exchange with the rate $r_x = r_{io} + r_{oi}$ [30] with the corresponding exchange time $\tau_x = 1/r_x$. Using the equilibrium condition and the normalization, $v_i + v_o = 1$,

$$r_x = r_{io} + r_{oi} = \frac{r_{io}}{v_o}. \quad (11)$$

The extracellular volume fraction lies in the range 0.20–0.25 from electrophoretic measurements [31]. The estimate of the intracellular volume fraction in the rat brain from the contrast agent suppression was 0.81 ± 0.08 [27]. This value gives the smallest $\tau_x = v_o \tau_{io}$ with $v_o \approx 0.19$. The most precise result of direct measurements [8], $\tau_{io} = 750 \pm 50$ ms turns then into an estimate $\tau_x \approx 140$ ms. It is still an order of magnitude larger than the recently obtained median value $\tau_x = 13$ ms [22].

To estimate the membrane permeability, we simulated the most precise preechange lifetime measurement in neurons from the rat cerebral cortex [8]. Figure 7 shows that the escape rate from the cells is not constant. Although the data are well fitted with a biexponential function,

$$S = S_0 \cdot (w_{\text{fast}} e^{-r_{\text{fast}} t} + w_{\text{slow}} e^{-r_{\text{slow}} t}), \quad (12)$$

we do not overload its parameters with any precise microstructural meaning. A fast-escape component with $\tau_{\text{fast}} \approx 50$ ms was also observed in the original study. It was however attributed to extracellular space because it showed a dependence on the flow rate of perfusate. The slow component was independent, which suggested the interpretation as the genuine permeation.

In line with that, we used the long-time exchange rate for interpreting experimental result. As expected, this rate is proportional to the membrane permeability, Fig. 8. Adjustment to the experimental value of $(750 \text{ ms})^{-1} = 0.0013 \text{ ms}^{-1}$ gave the membrane permeability $\kappa = 0.0036, 0.0057, 0.0046 \mu\text{m}/\text{ms}$ for the three cells, respectively Fig. 8.

We speculate that the admixture of extracellular space in the experiment [8] masked the true escape with τ_{fast} close to our finding in the idealized in silico conditions. The plausible explanation of the fast component is a rapid depletion of thin dendrites and the soma layer adjusted to the membrane. The following escape from the soma is slower being mediated by diffusion to the cell boundary

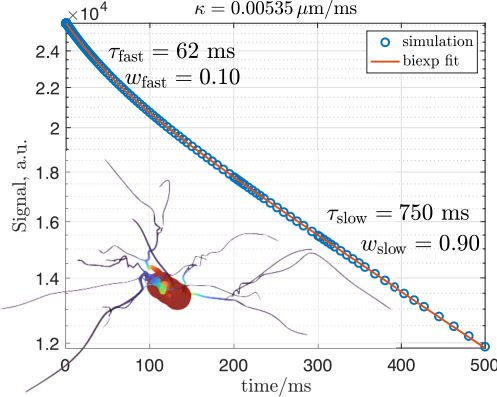


FIG. 7: Magnetization initially confined in cell 2 decreases due to permeation in extracellular space in which T_2 is very short. A biexponential function, Eq. (12), was fitted to computed data resulting in the parameters indicated in the image. The inset shows the cell's magnetization to the end time with the same colormap as in Fig. 2. The remaining magnetization in the soma is larger than in neurites. The membrane permeability was adjusted to match the measured preeexchange lifetime.

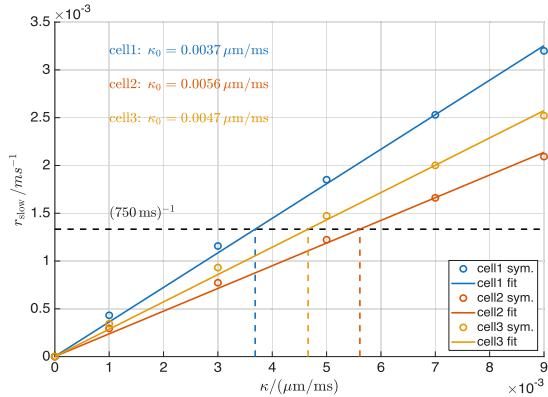


FIG. 8: The linear dependence between the long-time (slow) escape rate and the membrane permeability for three cells. The horizontal line shows the outcome of previous experiment [8]. Also shown are the values of membrane permeability that results in exactly this value in all cells. The zero escape rate at $\kappa = 0$ was forced in fitting.

and dendrites. This picture is supported by the higher magnetization in the soma to the end of the considered time interval (Fig. 7). Note that the preeexchange lifetime around 60 ms agrees with the cylinder model having a typical dendrite caliber $\approx 1 \mu\text{m}$ and the membrane permeability $\kappa = 0.005 \mu\text{m}/\text{ms}$. However, the signal fraction 10% of the fast component is smaller than the volume fraction of the neurites, which is 23% in cell 2. It prevents us from a too straightforward interpretation.

Summarizing, we assume the membrane permeability $\kappa = 0.005 \mu\text{m}/\text{ms}$ in what follows. An obvious drawback of our approach is the missing information about the cell geometry in the original measurements [8].

C. FEXI in permeable cells

Simulating exchange in the whole neural tissue requires a number of cells with a volume fraction around 80% with the rest volume attributed to extracellular space. Since we do not have such a comprehensive digitalized tissue at hand, the addition of ECS occurs in a semi-numerical way using the exchange model of Eq. (10). This model is applied to a single cell with an adjacent ECS. The latter is assigned the volume fraction $v_o = 0.2$ and the Gaussian diffusion with $D_{\text{ecs}} = 0.8 \mu\text{m}^2/\text{ms}$. The central quantity, $M(t) = [M_i(t), M_o(t)]^\dagger$ has a dual interpretation. When found with no applied gradient, it is the normalized magnetization, which coincides with the normalized amount of spins. The normalization implies $M_i(t) + M_o(t) = 1$ for both quantities. We use this approach to find fractions of migrating spins. Addition of field gradients decouples these quantities as described below.

The analytical solution to Eq. (10) takes the form

$$M(t) = \frac{1}{z+1} \begin{pmatrix} z + e^{-r_x t} \\ 1 - e^{-r_x t} \end{pmatrix}, \quad (13)$$

where the top and bottom components are M_i and M_o , respectively. Here r_x is the exchange rate, Eq. (11), and z is the ratio of volume fractions, $z = v_i/v_o$. The initial condition for this solution selects the spins located exclusively inside the cell, $M(0) = [1, 0]^\dagger$.

Our simulation package can treat a cell embedded in a large box, which implies $z = 0$ in Eq. (13). We find numerically the fraction of spins remaining in the cell, $M_i^{(0)}(t)$ and replace the exponential in Eq. (13) with this quantity.

So obtained $M(t)$ is the fraction of spins remaining in the cell with account for the reverse flow from a limited ECS. It is the first of four groups of spins that contribute to the final diffusion coefficients $D(t)$. The groups are: (i) “the resident” that stay in the cell to the end of mixing time. Their contribution to $D(t)$ is found numerically; (ii) “The emigrants” that leave the cell to ECS. The spin fraction is $1 - M(t)$ with the filter effect found numerically in the cell geometry, and the detection block giving the value D_{ecs} ; (iii) “The immigrants” that move from ECS in the cell. Since the overall spin density is constant, the fraction of this group is also $1 - M(t)$. The filter effect is $e^{-b_f D_{\text{ecs}}}$ and the contribution to $D(t)$ is found numerically; (iv) “the foreigners” that stay in ECS. The spin fraction is the original v_o minus the “immigrants”. The filter effect and the outcome of the detection block are both defined by D_{ecs} .

The final $D(t)$ is the mean over the four groups weighted with their spin fractions and the filter effect. It is shown in Fig. 9. Considering the practically achievable mixing times, the effect of finite membrane permeability is negligible for $t_m \ll \tau_x \approx 140 \text{ ms}$. It becomes noticeable when

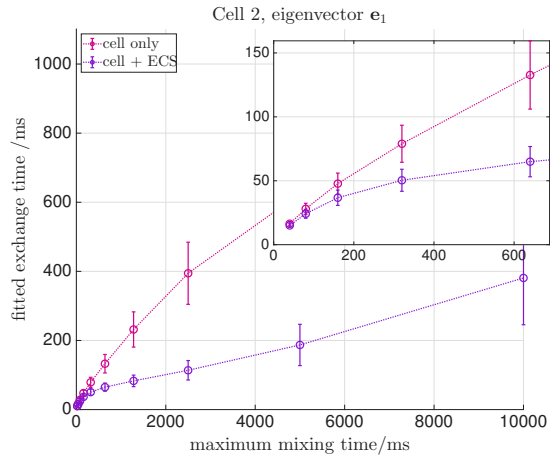


FIG. 9: Effect of added extracellular space on fitted exchange time, τ_x . Red line shows results as in Fig. 4, here for cell 2. Purple line shows results for added ECS as explained in the text. The initial values equal 10.4 ms for both lines with a rapidly increasing difference on the scale of a hundred of milliseconds.

both times are comparable.

D. Limitations

Beyond the already mentioned data insufficiency, the considered digitalized cells do not include any fine structure such as spines. This should not be a major problem because of their small size of the order of a micrometer. We anticipate that diffusion coarse-grains such feature during the characteristic time of a few milliseconds resulting in effective dendrite size and diffusivity. Such a renormalization should not change our results essentially.

We note also the absence of any structure inside the soma that can contribute to some increase in the preeexchange lifetime.

V. CONCLUSIONS

How to reconcile the broad band of experimental finding for the exchange time? The experimental setup with the suppression of extracellular signal suggests that the preeexchange lifetime is immune to intracellular motion thus reflecting the *genuine membrane permeation*. In contrast, diffusion-based measurements such as FEXI are sensitive to any change in the local diffusivity of spins, in other words to both the true permeation and to geometric exchange. The relative contribution of these processes depends on time sampled in an experiment. For short times, the fastest process dominates. According to our interpretation of cell culture experiment [8], the true permeation has a characteristic time about 140 ms. Therefore, an order of magnitude shorter exchange times,

such as $\tau_x \approx 13$ ms [22] should be attributed to the *geometric exchange inside* ramified cells.

Of course, this is currently a hypothesis, since the short exchange time was obtained with NEXI [32, 33], the standard model of white matter [1] supplemented with exchange. Hypothesis validation for this method is the topic of nearest future.

Focusing on FEXI, a way to validate the present results could be an observation of essentially multiexponential recovery of the filter-suppressed diffusion coefficient, similar to the simulated results shown in Figs. 3 and 4.

ACKNOWLEDGMENTS

We are indebted to Joseph J. Ackerman and Dmitry S. Novikov for stimulating discussions. We are grateful to the Engineering for Health (E4H) interdisciplinary center of Institut Polytechnique de Paris, and the “Biomedical Engineering Seed Grant Program” funded by the Fondation Bettencourt Schueller.

Appendix A

1. Magnetization during the mixing time

We describe here the evolution of longitudinal magnetization during the mixing time. The problem is effectively one-dimensional as $\rho \ll L$. The general solution is

$$\psi(t, x) = \sum_{n=0}^{\infty} C_n \psi_n(x) e^{-\lambda_n t}, \quad (\text{A1})$$

where $\psi_n(x)$ are the eigenfunctions of the Laplace operator $-D \partial^2 / \partial x^2$ with the eigenvalues λ_n and the coefficients C_n being the projections of the initial magnetizations on $\psi_n(x)$. For the problem at hand, x is the straightened distance along the cylinders, $-L/2 < x < L/2$.

The eigenfunctions are well known,

$$\begin{aligned} \psi_0(x) &= \sqrt{\frac{1}{L}}, \quad \lambda_0 = 0 \\ \psi_n(x) &= \sqrt{\frac{2}{L}} \sin k_n x, \quad k = \frac{(2n-1)\pi}{L}, \quad \lambda_n = D_0 k_n^2, \\ n &= 1, 2, 3 \dots \end{aligned} \quad (\text{A2})$$

Not written here are the even functions, proportional to $\cos p_n x$. These function do not enter the result by symmetry and the orthogonality to ψ_0 .

The initial conditions read to the first approximation

$$\psi(0, x) = \begin{cases} e^{-b_f D_0} & \text{for } -\frac{L}{2} < x < 0 \\ 1 & \text{for } 0 < x < \frac{L}{2} \end{cases}. \quad (\text{A3})$$

according to Eq. (2). To use the symmetry of the bent cylinder, we express this initial magnetization in terms of the even and odd components,

$$\psi_{\text{even}}^{(0)} = \frac{1 + e^{-b_f D_0}}{2} \quad (\text{A4})$$

$$\psi_{\text{odd}}^{(0)} = \frac{1 - e^{-b_f D_0}}{2} \text{sgn } x, \quad (\text{A5})$$

where $\text{sgn } x = x/|x|$ is the sign of x . The initial condition is then $\psi(0, x) = \psi_{\text{even}}^{(0)} + \psi_{\text{odd}}^{(0)}$. By the linearity of diffusion equation, the solution $\psi(t, x)$ is the sum of two solutions with the initial conditions $\psi_{\text{even}}^{(0)}$ and $\psi_{\text{odd}}^{(0)}$. The former excites the constant ψ_0 only. The odd part excites all odd modes, Eq. (A2), with $C_n = \sqrt{2/L}/k_n$. Summarizing,

$$\psi(t, x) = \psi_{\text{even}}^{(0)} + |\psi_{\text{odd}}^{(0)}| \frac{4}{L} \sum_{n=1}^{\infty} \frac{\sin k_n x}{k_n} e^{-D_0 k_n^2 t}. \quad (\text{A6})$$

Separate integrations over the two shoulder result in Eqs. (6) and (7).

2. Short-time approximation

The general solution, Eq. (A1), can be written in terms of the propagator (the Green's function) of diffusion equation, $G(t, x, x_0)$,

$$\psi(t, x) = \int_{-L/2}^{L/2} dx G(t, x, x_0) \psi(0, x_0). \quad (\text{A7})$$

This exact solution becomes approximate when the propagator is treated as the free one

$$G(t, x, x_0) \approx G_0(t, x - x_0) = \frac{e^{-(x-x_0)^2/(4D_0 t)}}{\sqrt{4\pi D_0 t}}, \quad (\text{A8})$$

which is possible for $\sqrt{D_0 t} \ll L$. Calculating the integral in the limit $L \rightarrow \infty$ with the initial condition of Eq. (2) results in Eq. (8).

[1] Dmitry S Novikov, Els Fieremans, Sune N Jespersen, and Valerij G Kiselev. Quantifying brain microstructure with diffusion MRI: Theory and parameter estimation. *NMR Biomed*, 32(4):e3998, 04 2019.

[2] Ingrid Åslund and Daniel Topgaard. Determination of the self-diffusion coefficient of intracellular water using PGSE NMR with variable gradient pulse length. *Journal of Magnetic Resonance*, 201(2):250–254, 2009.

[3] Samo Lasić, Markus Nilsson, Jimmy Lätt, Freddy Ståhlberg, and Daniel Topgaard. Apparent exchange rate mapping with diffusion MRI. *Magnetic Resonance in Medicine*, 66(2):356–365, 2011.

[4] Markus Nilsson, Jimmy Lätt, Danielle van Westen, Sara Brockstedt, Samo Lasić, Freddy Ståhlberg, and Daniel Topgaard. Noninvasive mapping of water diffusional exchange in the human brain using filter-exchange imaging. *Magn Reson Med*, 69(6):1573–81, Jun 2013.

[5] Ying Qiao, Petrik Galvosas, Thorsteinn Adalsteinsson, Monika Schönhoff, and Paul T Callaghan. Diffusion exchange NMR spectroscopic study of dextran exchange through polyelectrolyte multilayer capsules. *The Journal of chemical physics*, 122(21):214912, 2005.

[6] Diana Bernin and Daniel Topgaard. NMR diffusion and relaxation correlation methods: New insights in heterogeneous materials. *Current opinion in colloid & interface science*, 18(3):166–172, 2013.

[7] Mohammad Khateri, Marco Reisert, Alejandra Sierra, Jussi Tohka, and Valerij G. Kiselev. What does FEXI measure? *NMR in Biomedicine*, n/a(n/a):e4804, 2022.

[8] Donghan M Yang, James E Huettner, G Larry Bretthorst, Jeffrey J Neil, Joel R Garbow, and Joseph J H Ackerman. Intracellular water preeexchange lifetime in neurons and astrocytes. *Magn Reson Med*, 79(3):1616–1627, Mar 2018.

[9] Carolina Tecuatl, Bengt Ljungquist, and Giorgio A. Ascoli. Accelerating the continuous community sharing of digital neuromorphology data. *FASEB BioAdvances*, 6(7):207–221, 2024.

[10] NeuroMorpho.Org. (RRID:SCR_002145). <https://neuromorpho.org>.

[11] Alex McSweeney-Davis, Chengran Fang, Emmanuel Caruyer, Anne Kerbrat, and Jing-Rebecca Li. Alpha_mesh_swc: automatic and robust surface mesh generation from the skeleton description of brain cells. *Briefings in Bioinformatics*, 26(3):bbaf258, 06 2025.

[12] Hang Si. Tetgen, a delaunay-based quality tetrahedral mesh generator. *ACM Trans. Math. Softw.*, 41(2), February 2015.

[13] Jing-Rebecca Li, Van-Dang Nguyen, Try Nguyen Tran, Jan Valdman, Cong-Bang Trang, Khieu Van Nguyen, Duc Thach Son Vu, Hoang An Tran, Hoang Trong An Tran, and Thi Minh Phuong Nguyen. Spindocitor: A MATLAB toolbox for diffusion MRI simulation. *NeuroImage*, 202:116120, 2019.

[14] Chengran Fang, Van-Dang Nguyen, Demian Wassermann, and Jing-Rebecca Li. Diffusion mri simulation of realistic neurons with SpinDoctor and the Neuron Module. *NeuroImage*, 222:117198, 2020.

[15] Jing-Rebecca Li, Try Nguyen Tran, and Van-Dang Nguyen. Practical computation of the diffusion mri signal of realistic neurons based on laplace eigenfunctions. *NMR in Biomedicine*, 33(10):e4353, 2020. e4353 nbm.4353.

[16] Bibek Dhital, Marco Reisert, Elias Kellner, and Valerij G Kiselev. Intra-axonal diffusivity in brain white matter. *NeuroImage*, 189:543–550, Jan 2019.

[17] Karli K Watson, Todd K Jones, and John M Allman. Dendritic architecture of the von Economo neurons. *Neuroscience*, 141(3):1107–1112, 2006.

[18] Bob Jacobs, Matthew Schall, Melissa Prather, Elisa Kapler, Lori Driscoll, Serapio Baca, Jesse Jacobs, Kevin Ford, Marcy Wainwright, and Melinda Treml. Regional dendritic and spine variation in human cerebral cortex: a quantitative golgi study. *Cerebral Cortex*, 11(6):558–571, 06 2001.

[19] Jing-Rebecca Li, Try Nguyen Tran, and Van-Dang Nguyen. Practical computation of the diffusion MRI signal of realistic neurons based on Laplace eigenfunctions. *NMR in Biomedicine*, 33(10):e4353, 2020. e4353 nbm.4353.

[20] Els Fieremans, Dmitry S Novikov, Jens H Jensen, and Joseph A Helpern. Monte carlo study of a two-compartment exchange model of diffusion. *NMR Biomed*, 23(7):711–24, Aug 2010.

[21] Chenyang Li, Els Fieremans, Dmitry S Novikov, Yulin Ge, and Jiangyang Zhang. Measuring water exchange on a preclinical MRI system using filter exchange and diffusion time dependent kurtosis imaging. *Magn Reson Med*, 89(4):1441–1455, Apr 2023.

[22] Kwok-Shing Chan, Yixin Ma, Hansol Lee, José P Marques, Jonas Olesen, Santiago Coelho, Dmitry S Novikov, Sune Jespersen, Susie Y Huang, and Hong-Hsi Lee. In vivo human neurite exchange imaging (NEXI) at 500 mT/m diffusion gradients. *bioRxiv : the preprint server for biology*, page 2024.12.13.628450, Dec 2024.

[23] Gheorghe Benga. Water transport in red blood cell membranes. *Progress in Biophysics and Molecular Biology*, 51(3):193–245, 1988.

[24] G Benga, V I Pop, O Popescu, and V Borza. On measuring the diffusional water permeability of human red blood cells and ghosts by nuclear magnetic resonance. *J Biochem Biophys Methods*, 21(2):87–102, 1990.

[25] R. David Andrew, Mark W. Labron, Susan E. Boehnke, Lisa Carnduff, and Sergei A. Kirov. Physiological evidence that pyramidal neurons lack functional water channels. *Cerebral Cortex*, 17(4):787–802, 05 2006.

[26] Daniel Boss, Jonas Kühn, Pascal Jourdain, Christian Depeursinge, Pierre J Magistretti, and Pierre Marquet. Measurement of absolute cell volume, osmotic membrane water permeability, and refractive index of transmembrane water and solute flux by digital holographic microscopy. *J Biomed Opt*, 18(3):036007, Mar 2013.

[27] James D Quirk, G Larry Bretthorst, Timothy Q Duong, Avi Z Snyder, Charles S Springer, Jr, Joseph J H Ackerman, and Jeffrey J Neil. Equilibrium water exchange between the intra- and extracellular spaces of mammalian brain. *Magn Reson Med*, 50(3):493–499, Sep 2003.

[28] Ruiliang Bai, Charles S Springer, Jr, Dietmar Plenz, and Peter J Basser. Fast, Na^+ / K^+ pump driven, steady-state transcytolemmal water exchange in neuronal tissue: A study of rat brain cortical cultures. *Magn Reson Med*, 79(6):3207–3217, 06 2018.

[29] J.R. Zimmerman and W.E. Brittin. Nuclear magnetic resonance studies in multiple phase systems: Lifetime of a water molecule in an adsorbing phase on silica gel. *The Journal of Physical Chemistry*, 61(10):1328–1333, 1957.

[30] PT Callaghan and I Furó. Diffusion-diffusion correlation and exchange as a signature for local order and dynamics. *J Chem Phys*, 120(8):4032–8, Feb 2004.

[31] Eva Syková and Charles Nicholson. Diffusion in brain extracellular space. *Physiol Rev*, 88(4):1277–340, Oct 2008.

[32] Ileana O Jelescu, Alexandre de Skowronski, Françoise Geffroy, Marco Palombo, and Dmitry S Novikov. Neurite exchange imaging (NEXI): A minimal model of diffusion in gray matter with inter-compartment water exchange. *Neuroimage*, 256:119277, Aug 2022.

[33] Jonas L Olesen, Leif Østergaard, Noam Shemesh, and Sune N Jespersen. Diffusion time dependence, power-law scaling, and exchange in gray matter. *NeuroImage*, 251:118976, 05 2022.